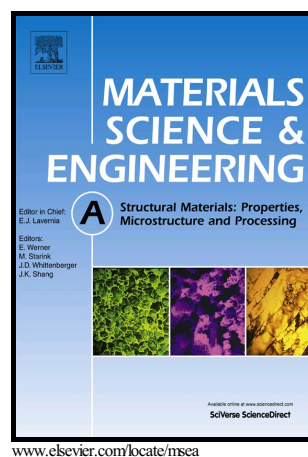


Vacancy effects on the mechanical behavior of B2-FeAl intermetallics

M. Zamanzade, G. Hasemann, C. Motz, M. Krüger, A. Barnoush



PII: S0921-5093(17)31515-0
DOI: <https://doi.org/10.1016/j.msea.2017.11.054>
Reference: MSA35769

To appear in: *Materials Science & Engineering A*

Received date: 13 June 2017
Revised date: 14 November 2017
Accepted date: 15 November 2017

Cite this article as: M. Zamanzade, G. Hasemann, C. Motz, M. Krüger and A. Barnoush, Vacancy effects on the mechanical behavior of B2-FeAl intermetallics, *Materials Science & Engineering A*, <https://doi.org/10.1016/j.msea.2017.11.054>

This is a PDF file of an unedited manuscript that has been accepted for publication. As a service to our customers we are providing this early version of the manuscript. The manuscript will undergo copyediting, typesetting, and review of the resulting galley proof before it is published in its final citable form. Please note that during the production process errors may be discovered which could affect the content, and all legal disclaimers that apply to the journal pertain.

Vacancy effects on the mechanical behavior of B2-FeAl intermetallics

M. Zamanzade^{a*}, G. Hasemann^b, C. Motz^a, M. Krüger^b, A. Barnoush^{a,c}

^aDepartment of Materials Science, Saarland University, Bldg. D22, 66041 Saarbrücken, Germany

^bInstitute of Materials and Joining Technology, Otto-von-Guericke University, Magdeburg, Universitätsplatz 2, 39106 Magdeburg, Germany

^cDepartment of Engineering Design and Materials, Norwegian University of Science and Technology, No-7491 Trondheim, Norway

*Corresponding authors. m.zamanzade@matsci.uni-sb.de

Abstract

The present work addresses the impact of quenched-in thermal vacancies on the mechanical properties of B2 iron aluminides. For this reason different binary Fe-Al alloys with different histories of heat treatment were indented at room temperature. The contributions of mono- and bi-vacancies in addition to triple defects on the elastic, plastic and elastic-plastic transition were evaluated using nanoindentation technique. In the samples containing bi-vacancies, the increase of the hardness was much more pronounced compared to the mono-vacancies.

Keywords: hardness; micromechanics; stress/strain measurements; intermetallics; iron alloys; plasticity

List of Symbols

b	magnitude of the Burgers vector
C_V	vacancy concentration
E_r and E	reduced elastic modulus measured by the Oliver-Pharr method and experimentally measured elastic modulus
F_p	cumulative probability of pop-in event
H and ΔH	depth dependent hardness and the change in hardness due to the thermal defects
h and h_c	measured displacement and contact depth

K	constant
k_B	Boltzmann constant
M	Tabor's constant
\dot{n} and \dot{n}_0	rate of dislocation nucleation and attempt frequency per unit volume
P and $P_{\text{pop-in}}$	applied load and pop-in load
R	tip radius
T	absolute temperature
V	the volume of the region beneath the tip where a defined percentage of the maximum shear stress is acting
V_A	activation volume
$w_{\text{pop-in}}$	Width of pop-in
z_{max}	a certain depth with the maximum shear stress while pop-in happens
α	angle between the surface of the indenter and the surface plane of the indented material
β	constant
χ	constant
$\dot{\epsilon}$	strain rate
ϵ	required activation energy for the dislocation nucleation
ϕ	Taylor coefficient which is between 0.1-0.5 depending on dislocation structures
μ	shear modulus
σ , σ_f and σ_{flow}	externally applied stress, flow stress not accounting for the effect of the intrinsic lattice resistance and macroscopic flow stress in uniaxial compression test (~0.2 plastic strain was used in this work)
τ_{13} , τ_{max} , $\tau_{\text{P-N}}$ and τ_v	transverse shear stress, maximum applied shear stress, friction stress and friction component caused by the existence of vacancies

1 Introduction

FeAl and Fe₃Al intermetallics are promising candidates for structural and high-temperature applications such as gas turbines or automobile engine components[1,2]. Iron aluminides combine excellent high-temperature oxidation resistance with a high melting point, a lower density and potentially lower costs in comparison to austenitic stainless steels[3]. One important issue with iron aluminides is their high concentrations of vacancies, or anti-sites, which influence thermo-mechanical, magnetic and electrical properties in addition to the yield strength anomaly of the intermetallics [4-6]. Increase of Al concentration and/or temperature raises the vacancy concentration (Fig. 1). High

concentration of vacancies and anti-sites enhance the interaction of the point defects and formation of defect clusters. Fig. 2c and d schematically show two typical clusters of point defects, namely bi-vacancies or triple defects in a B2 super lattice. Köster and Gödecke first reported a different endothermic and exothermic behavior of iron aluminides at concentrations between 36 and 52 at.% Al during heating and cooling. They observed different high and low temperature states of the B2 phase (B2(h) and B2(l), respectively) by measuring the thermal expansion, susceptibility and elastic modulus [7-11]. Later, their findings were considered in assessment of the Fe-Al phase diagram, i.e., by Kubashewski [12] and Stein et al. [13]. In the ordered B2 phase with less than 35 at.% Al (refers as B2' [13]), the type of point defects at low temperatures is mostly mono-vacancies. In the aluminides with Al content between 36 and 52 at.%, the type of the most stable defects change from triple defects at low temperature to bi-vacancies at higher temperatures[13].

Vacancies have a strengthening effect and typically increase the hardness of metals [14-16]. In line with this fact, a strong dependence of yield strength of Fe₃Al on heat treatment has been reported [17,18], which shows a similar strengthening effect in D0₃-structured iron aluminides as in FeAl alloys. The contribution of the vacancies to the strengthening in ordered intermetallics can be described through various hardening mechanisms, e.g. the barrier effect of vacancies for dislocation movement, classic solid solution strengthening [15,19], precipitation strengthening[20], anti-phase domains (APD) and long range order (LRO) [21] as well as anti-site defect strengthening [22,23]. The contribution of these mechanisms to the room temperature strength has been reviewed recently [18]. In this paper the contributions of mono-vacancies and also clusters of point defects to different nano-mechanical properties (e.g. elastic modulus, dislocation nucleation mechanism and strengthening effect) were studied via nanoindentation technique. Nanoindentation technique has been used widely over the last decades for evaluating the mechanical properties of a large variety of materials at very small scales. One advantage of nanoindentation is its ability for collecting a significant number of results in a quite small sample volume by simple analyses of indentation load-displacement data [24,25]. Additionally, due to the small volume of the

tested sample, other types of lattice defects (e.g. grain boundaries) or material inhomogeneity (e.g. distribution of crystal orientations) does not influence the results.

2 Experimental procedure

A polycrystalline Fe-30 at.%Al and two single crystals (Fe-40 at.%Al and Fe-45 at.%Al) were used in this work. High-purity iron and aluminum metal chips were used for the preparation of Fe-30 at.%Al using arc melting for several times in an argon protecting atmosphere to guarantee homogeneity of samples; afterward they were drop-casted into a cylindrical copper mold with a diameter of 25.4 mm. The ingot was hot extruded with a 9:1 area reduction at 800 °C in a carbon steel. The extruded alloy was cut into 75 mm long rods, annealed at 1100 °C for 1 h in air and air-cooled to obtain homogenized samples. The grain size of Fe-30 at.%Al samples were measured to be ~600 μm by using the line intersect method in a Zeiss Jenaphot 2000 stereo light microscope. Earlier results did not reveal any detectable amounts of second phases in the samples [17].

After air-cooling, two slices were cut from the Fe-30 at.%Al rod, each having a diameter of 12 mm and a thickness of 6 mm using electro-discharge machining (EDM). The slices were annealed in the B2 phase field of the Fe-Al system either at 900 °C/24h or 600 °C/2days and quenched into water. The Fe-40 at.%Al and Fe-45 at.%Al samples were annealed in the B2 phase field of the Fe-Al system either at 900 °C/24h or 400 °C/4days and quenched into water to freeze-in thermal vacancies. The annealing time was increased with decreasing temperature because of slow vacancy annihilation kinetics at low temperatures. The criteria we used for the selection of quench temperatures were i) having B2 super structure in all cases and ii) in samples with the same Al content, enlarging the difference between the vacancy content in samples based on the Fe-Al phase diagram [4]. Table 1 presents the expected types of vacancies after each heat treatment [26-28].

After the heat treatment, the specimens were polished down to 1 μm with diamond suspension and then electro-polished with a 1M sulfuric acid-methanol solution [24,25,29] to remove mechanical damage near the surface [30]. When examined with atomic force microscopy (AFM), the average root-mean-square roughness of the samples was less than 1 nm over 100 μm^2 area.

The electron backscatter diffraction (EBSD) method was used for characterizing different crystal orientations of polycrystalline Fe-30 at.%Al samples. Grains with orientations close to (001) were selected and marked by means of micro-indenters. Nanoindentation was performed on selected, freshly electro-polished grains at room temperature. The big grain sizes in the case of polycrystalline samples make it possible to perform at least 200 nanoindentations on each grain. The nanoindenters were performed using a Hysitron TriboIndenter with a Performech™ controller. We used a conical diamond tip with a cone angle of 120° and a tip radius of 1270 nm in addition to a Berkovich tip with a radius of 450 nm. Tip radii were measured with the aid of the method explained in reference [24].

Additionally, micro-hardness tests were carried out using a Leica VMHT MOT micro-hardness tester equipped with a Vickers indenter and an optical light microscope. To achieve different indentation depths, the hardness was measured as a function of applied loads of 0.490, 2.940 and 19.610 N.

In order to compare the local measurements with the macroscopic behavior of alloys, the yield strength of quenched Fe-30 at.%Al was measured using room temperature compression tests. Cylindrical specimens with a diameter of 4 mm and a height of 6 mm were first cut by EDM. After annealing and quenching them in water, three samples for each quench temperature were compressed with a screw-driven TIRAtest 28100 testing device and a constant crosshead speed corresponding to an initial (engineering) strain rate of $\dot{\epsilon} = 10^{-3} \text{ s}^{-1}$. Yield strengths were measured based on the 0.2 % offset method. The results do not differ more than $\pm 30 \text{ MPa}$.

3 Results and discussions

Effect of vacancies on the elastic modulus and pop-in event

The specimen surface conditions including surface roughness and density of dislocations are very critical issues for nanoindentation. For various samples with different histories of heat treatment, the surface roughness was measured with the scanning mode of TriboIndenter. Due to the small contact area between nanoindenter and surface, there is a good possibility that the area below the indenter tip is small enough to be dislocation-free. This is the reason why purely elastic interaction is observed during the loading

segment until the dislocation nucleation happens (Fig. 3a and b). The deformation before the pop-in load (the critical load that causes the yielding of a material) follows the Hertzian contact model (Eq. 1) [31,32]:

$$P = \frac{4}{3} E_r R^{0.5} h^{1.5} \quad \text{Eq. 1}$$

Here P , E_r , R and h are applied load, reduced elastic modulus, tip radius and measured displacement respectively. The results show that the E_r of samples with 30 at.% Al vary from 162 ± 3 to 161 ± 4 GPa with increasing quenching temperature. In the case of samples with 45 at.% Al, the slight systematic decrease of the elastic modulus with the increase of the vacancy content ranges from 170 ± 2 to 167 ± 2 GPa. Heat treatment has a greater impact on the incipient plasticity and the post yielding behavior of the intermetallics compared to the elastic properties of materials. A statistical approach (cumulative distribution) from all performed indents is taken to clarify the effect of the quenching temperature on the pop-in load of Fe-45 at.%Al samples (Fig. 4a). The nucleation of a dislocation is a stress-assisted, thermally activated process [33]. In other words, the energy barrier for dislocation nucleation could be overcome by the mechanical work of indentation and simultaneously by an appropriate thermal fluctuation. The thermal fluctuations may sometimes favor dislocation nucleation and sometimes work against it. This is the reason for the observed scatter in the pop-in event. Hence, within a given load range, we can talk about the probability of the pop-in event. New experiments propose dislocation nucleation at the pre-existing vacancies [34]. Mainly based on simulations [35-37], it was shown that an increasing concentration of vacancies can ease the nucleation of dislocations, which results in a lower yield stress. An increase of the quenching temperature increases the concentration of vacancies and may change the type of defect cluster. It promotes earlier displacement bursts in the Fe-45 at.%Al and hence a shift to lower loads in the population of $P_{\text{pop-in}}$. For the sample with 30 at.% Al the tendency was the opposite (Fig. 4b). In order to validate this observation, nanoindentation was additionally performed with a conical indenter. It showed the same trend as a sharp Berkovich tip. With the increase of the loading rate, the pop-in load apparently increases (Fig. 4b). This is due to the fact that the probability of overcoming the energy barrier by thermal fluctuations decreases, since the time to reach the pop-in load decreases. In

contrast to the dependency of the pop-in load on the loading rate, no changes in the elastic modulus were observed for different loading rates. In appendix A, activation energies and volumes for different samples with different histories of heat treatment are calculated.

The probability of the existence of a vacancy beneath the tip

Based on the Hertzian contact model, the maximum shear stress below the tip (τ_{\max}) at pop-in load ($P_{\text{pop-in}}$) can be analytically calculated using Eq. 2 [31,32]:

$$\tau_{\max} = 0.31 \left(\frac{6P_{\text{pop-in}} E_r^2}{\pi^3 R^2} \right)^{1/3} \quad \text{Eq. 2}$$

High maximum shear stress, slightly lower than the theoretical values for dislocation nucleation ($\approx \mu/4\pi$ for Fe-30 at.%Al and $\approx \mu/3\pi$ for Fe-45 at.%Al), was detected in all samples with different histories of heat treatment (Fig. 5). The increment of the Al content in the alloys enhances τ_{\max} . This could be related to the enhancement of the interatomic potential, as suggested by Rose et al. [38-40]. It was analytically shown that the shear stress is maximum at a depth z_{\max} defined by [32]:

$$z_{\max} = 0.48 \left[\frac{3P_{\text{pop-in}} R}{4E_r} \right]^{1/3} \quad \text{Eq. 3}$$

Furthermore, it is possible to estimate the volume of the region where a defined percentage of the maximum shear stress is acting [32,41], which has a spheroid form (Fig. 6a). The change of the stressed volume in relation to the normalized applied shear stress is plotted in Fig. 6b. V and the total number of atoms in this volume are shown in Fig. 6c and d. Considering the average concentration of vacancies in the materials (table 1) and calculated V , the probability of encountering a vacancy beneath the tip in a highly strained lattice is very high.

In iron aluminides with Al well below the stoichiometry, we can *assume* that the lattice consists of randomly mixed Fe-bcc with perfect B2 unit cells (Fig. 7). In this situation, the question which may arise concerns the position of the mono-vacancies. In a stoichiometric B2 super-lattice, extremely high formation energy of mono-vacancies at

the Al sublattice makes the formation of this type of defect almost impossible[4]. Furthermore, while the formation energies of vacancies in pure Fe-bcc are higher ($E_f \approx 1.4$ eV [42]) than the predicted energies for the B2 lattice ($E_f \approx 1.0$ eV [4]), we can conclude that the possibility of the vacancy formation at the Fe¹ sublattice should be higher than in the case of Fe² (Fig. 7). In this situation, the first leading super partial dislocation nucleates with higher probability at the Fe-Fe side while the Al-Fe has higher formation enthalpy [4]. The existence of a preferred direction for the dislocation nucleation reduces the probability of the dislocation formation at a defined shear stress and could be a reason for the increase of the observed pop-in load with increasing the concentration of mono-vacancies for Fe-30 at.%Al samples. Other possible reasons for the observed behavior for Fe-30 at.%Al are i) the annihilation of vacancies in the compression zone [43] or ii) influence of thermal vibrations which may play a larger role in comparison to the weakening effect of vacancies [37] which may not be relevant at room temperature.

Effect of vacancies on dislocation mobility

Vacancy content influences the pop-in width, i.e. the width of the discontinuity in the load-displacement curves. The $w_{\text{pop-in}}$ represents the ability of nucleated dislocations beneath the tip to slip. As shown in Fig. 8, the pop-in width (at a constant $P_{\text{pop-in}}$) decreases with increasing vacancy content in both samples. This is due to the reduction of the free path of a dislocation in the samples with higher vacancy concentration. It is a clear evidence for the barrier effect of the vacancies on the movement of the nucleated dislocations. Interestingly at a defined $P_{\text{pop-in}}$, the loading rate does not affect the $w_{\text{pop-in}}$; hence no effects of the loading rate on the motion of nucleated dislocations at this small indentation depth were observed.

Fig. 9a illustrates the hardness values obtained by nanoindentation and micro-indentation experiments. The hardness decrease with the increase of the indentation size at the sub-micrometer depths is known as the indentation size effect (ISE). At a constant depth of indentation (for a given tip geometry), the increase of hardness values presents a more sessile feature of dislocations. As a first approximation, we can formulate the dependency of hardness (H) on the indentation depth using the Nix and Gao[44] model:

$$H = 3 \left[\sqrt{\sigma_f^2 + \frac{9}{2h} \varphi^2 \mu^2 b \tan^2 \alpha} + \sqrt{3} (\tau_{p-N} + \tau_v) \right] \quad \text{Eq. 4}$$

Here b , σ_f , τ_{p-N} and τ_v are Burgers vector, flow stress not accounting for the effect of the intrinsic lattice resistance, friction stress and extra friction component caused by the existence of vacancies respectively. φ and α are constants. Since the elastic properties (and hence the shear modulus) are almost independent of C_v , the increase of the hardness should be mainly due to the contribution of vacancies to the friction of the dislocations. The other parameters in Eq. 4 are not influenced by the variation of C_v . The strengthening due to vacancies or other thermal defects is often described by the equation [23]:

$$\Delta H = 3K \cdot \sqrt{C_v} \quad \text{Eq. 5}$$

K is a constant which is estimated to be in the order of $\mu/30$ [23]. Based on this approximation, the effect of vacancy content on the hardness values is plotted in Fig. 9b. This approximation is in very good agreement with our experimental data in the case of Fe-30 at.%Al samples. However, Fig. 9b shows a strong deviation between the expected increase of hardness values in the case of Fe-40 at.% Al and Fe-45 at.% Al and the experimental results. It shows that the bi-vacancies influence the mobility of dislocation and hence hardness much more in comparison to the mono-vacancies. Therefore, the K value for bi-vacancies or triple defects should be assumed to be $\approx \mu/15$.

While the huge amounts of vacancies are not thermodynamically stable at room temperature, one may ask about vacancy concentration at the surface. In order to check the validity of our nano- and micro-mechanical testing methods, we evaluated the effect of C_v on macro-scale mechanical properties with the aid of compression tests. Fig. 10 summarizes the compression tests for Fe-30 at.%Al specimens quenched from 600 and 900 °C respectively. Additionally, a specimen was first quenched from 900 °C and then re-annealed at 600 °C to demonstrate the influence of vacancy migration and annihilation. Consistent with literature on vacancy migration kinetics [45], the yield strength could be recovered by re-annealing in the B2 phase field, reaching identical values as by quenching from a heat treatment of 600 °C/2days. The increase of the flow stress under uniaxial loading can be related to the changes of measured hardness values by the application of the Tabor's relation $\Delta H = M\Delta\sigma_{flow}$ ($M \sim 3$). Good agreement between microscopic and macroscopic measurements guarantees the homogeneous distribution of vacancies in bulk materials.

Conclusions

Our results show that

- 1: for samples with the same histories of heat treatment, an increase of Al content from 30 at.% to 45 at.% enhances elastic modulus, hardness and critical resolved shear stress needed for dislocation nucleation.
- 2: increase of vacancy content causes a slight reduction of the elastic modulus (in the case of samples with bi-vacancies) and simultaneously an enhancement of hardness. Bi-vacancies, however, increase the hardness values much more significantly in comparison to the mono-vacancies.
- 3: the critical resolved shear stress needed for dislocation nucleation decreases in the case of samples containing bi-vacancies. In contrast, the existence of mono-vacancies may increase the τ_{max} .

Acknowledgments

The authors wish to thank Dr. J. H. Schneibel from the Department of Materials Science and Technology, Oak Ridge National Laboratory and Prof. Dr. Horst Vehoff from the Department of Materials Science and Engineering, Saarland University for their help, guidance and invaluable comments. Moreover, the financial support by the DFG and the Methodisch-Diagnostisches Zentrum Werkstoffprüfung (MDZWP) e.V., Magdeburg, Germany is gratefully acknowledged.

Appendix A

Activation volume for dislocation nucleation

The nucleation rate of dislocations in a unit volume of material exposed to a uniform stress state can be formulated as follows [33,46-48]:

$$\dot{n} = \dot{n}_0 \exp\left[-\frac{\varepsilon - \sigma V_A}{k_B T}\right] \quad \text{Eq. 6}$$

The cumulative probability, F_p , correlates with the $P_{\text{pop-in}}$ via the Eq. 7 [47]:

$$\ln[-\ln(1 - F_p)] = \chi P^{1/3} + \beta \quad \text{Eq. 7}$$

By plotting $\ln[-\ln(1 - F_p)]$ versus $P^{1/3}$ as shown in Fig. 11, the experimental data follow approximately a linear tendency for data sets attained for different samples at different loading rates. The parameter χ is correlated with the V_A through Eq. 8 [47]:

$$V_A = \frac{\pi}{0.47} \left(\frac{3R}{4E_r} \right)^{2/3} k_B T \chi \quad \text{Eq. 8}$$

Hence, the activation energy can be calculated as follows:

$$\varepsilon = \tau_{\text{max}} V_A = k_B T \chi P^{1/3} \quad \text{Eq. 9}$$

The measured ε and V_A for different samples are presented in Fig. 12. Earlier, a very small activation volume for bcc-Cr was reported based on nanoindentation technique [34]. The calculated V_A was $(0.308 \pm 0.015) \times b^3$ which is about 4.81 \AA^3 . Furthermore, the micro-compression testing method was used for calculating the activation volume of single crystalline Mo-pillars with diameters of 200nm[49]. The calculated V_A was about

$1 \times b^3$. Our results show that the calculated activation volume for the samples quenched from low temperatures is also about $1 \times (b^*)^3$ while b^* is the Burgers vector of a super dislocation in the B2 super lattice ($b^* = 2b$). The increase of the activation volume in the binary samples with higher Al content (those which were quenched from low temperatures) should only be due to the enhancement of the lattice parameter and hence the Burgers vector in the Al-rich samples. A comparison of the results of the sharp Berkovich tip with those obtained by the blunt spherical tip (Fig 12a and c) unexpectedly shows the influence of the tip geometry on the calculated activation volume and consequently the activation energies. This is probably due to the simplified model used for the calculation of the mentioned items. Furthermore, a slight dependency of both ε and V_A on the loading rate (Fig 12c and d) was observed based on our experimental results. Another crucial point that should be mentioned is the increase of the activation volume in the case of samples quenched from 900°C. This increase is especially obvious in the case of Fe-45 at.%Al. The reason for this strong enhancement is not clear.

References

1. Liu, C.T.; George, E.P.; Maziasz, P.J.; Schneibel, J.H. Recent advances in b2 iron aluminide alloys: Deformation, fracture and alloy design. *Mat Sci Eng a-Struct* **1998**, 258, 84-98.
2. Mckamey, C.G.; Devan, J.H.; Tortorelli, P.F.; Sikka, V.K. A review of recent developments in Fe3Al-based alloys. *Journal of Materials Research* **1991**, 6, 1779-1805.
3. Zamanzade, M.; Barnoush, A. An overview of the hydrogen embrittlement of iron aluminides. *Procedia Materials Science* **2014**, 3, 2016-2023.
4. Zamanzade, M.; Barnoush, A.; Motz, C. A review on the properties of iron aluminide intermetallics. *Crystals* **2016**, 6.

5. George, E.P.; Baker, I. A model for the yield strength anomaly of Fe-Al. *Philos Mag A* **1998**, 77, 737-750.
6. George, E.P.; Baker, I. Thermal vacancies and the yield anomaly of FeAl. *Intermetallics* **1998**, 6, 759-763.
7. Koster, W.; Godecke, T. Physical measurements on iron-aluminum-alloys between 10 and 50 at percent Al .1. Confirmation of and additional contribution to the iron-aluminum phase-diagram. *Z Metallkd* **1980**, 71, 765-769.
8. Koster, W.; Godecke, T. Physical measurements on iron-aluminum-alloys between 10-at-percent and 50 at-percent Al .4. The modulus of elasticity of the alloys. *Z Metallkd* **1982**, 73, 111-114.
9. Koster, W.; Godecke, T. Physical measurements on iron-aluminum alloys between 10 and 50 at-percent Al .6. On a speciality of the thermal-expansion behavior of the FeAl high-temperature modification. *Z Metallkd* **1983**, 74, 705-708.
10. Godecke, T.; Koster, W. Physical measurements on iron-aluminium alloys between 10 and 50 at-percent Al.7. The thermal-expansion behavior on annealing of 26.5 to 50 at-percent Al-alloys quenched from decreasing furnace temperatures. *Z Metallkd* **1984**, 75, 161-169.
11. Koster, W.; Wachtel, E.; Godecke, T. Physical measurements on iron-aluminum alloys between 10 and 50 at-percent Al .9. Statements about constitution of iron-alloys with 38 to 50 at-percent Al by means of susceptibility measurements. *Z Metallkd* **1985**, 76, 382-387.
12. Kubaschewski, O. *Iron—binary phase diagrams*. Springer Science & Business Media: 2013.

13. Stein, F.; Palm, M. Re-determination of transition temperatures in the Fe-Al system by differential thermal analysis. *Int J Mater Res* **2007**, 98, 580-588.
14. Baker, I.; Munroe, P.R. Mechanical properties of FeAl. *Int Mater Rev* **1997**, 42, 181-205.
15. Herrmann, J.; Inden, G.; Sauthoff, G. Deformation behaviour of iron-rich iron-aluminium alloys at high temperatures. *Acta Materialia* **2003**, 51, 3233-3242.
16. Herrmann, J.; Inden, G.; Sauthoff, G. Deformation behaviour of iron-rich iron-aluminum alloys at low temperatures. *Acta Materialia* **2003**, 51, 2847-2857.
17. Hasemann, G.; Schneibel, J.H.; George, E.P. Dependence of the yield stress of Fe₃Al on heat treatment. *Intermetallics* **2012**, 21, 56-61.
18. Hasemann, G.; Schneibel, J.H.; Krüger, M.; George, E.P. Vacancy strengthening in Fe₃Al iron aluminides. *Intermetallics* **2014**, 54, 95-103.
19. Morris, D.G.; Munoz-Morris, M.A.; Requejo, L.M. Work hardening in Fe-Al alloys. *Mat Sci Eng a-Struct* **2007**, 460, 163-173.
20. Morris, D.G.; Gunther, S. Room and high temperature mechanical behaviour of a Fe₃Al-based alloy with α - α'' microstructure. *Acta Materialia* **1997**, 45, 811-822.
21. Leamy, H.J.; Kayser, F.X. Compressive deformation behavior of long range ordered polycrystalline iron-aluminum alloys. *Phys Status Solidi* **1969**, 34, 765-&.
22. Kogachi, M.; Haraguchi, T. Quenched-in vacancies in b2-structured intermetallic compound FeAl. *Materials Science and Engineering: A* **1997**, 230, 124-131.

23. Pike, L.M.; Chang, Y.A.; Liu, C.T. Point defect concentrations and hardening in binary B2 intermetallics. *Acta Materialia* **1997**, *45*, 3709-3719.
24. Zamanzade, M.; Vehoff, H.; Barnoush, A. Effect of chromium on elastic and plastic deformation of Fe₃Al intermetallics. *Intermetallics* **2013**, *41*, 28-34.
25. Barnoush, A.; Zamanzade, M. Effect of substitutional solid solution on dislocation nucleation in Fe₃Al intermetallic alloys. *Philos Mag* **2012**, *92*, 3257-3268.
26. Hehenkamp, T.; Scholz, P.; Kohler, B.; Kerl, R. Vacancy formation and diffusion in FeAl-alloys. *Defect Diffus Forum* **2001**, *194-1*, 389-395.
27. Wurschum, R.; Grupp, C.; Schaefer, H.E. Simultaneous study of vacancy formation and migration at high-temperatures in B2-type Fe aluminides. *Physical Review Letters* **1995**, *75*, 97-100.
28. Schneibel, J.H. Strengthening of iron aluminides by vacancies and/or nickel. *Mat Sci Eng a-Struct* **1998**, *258*, 181-186.
29. Zamanzade, M.; Vehoff, H.; Barnoush, A. Cr effect on hydrogen embrittlement of Fe₃Al-based iron aluminide intermetallics: Surface or bulk effect. *Acta Materialia* **2014**, *69*, 210-223.
30. Wang, Z.G.; Bei, H.; George, E.P.; Pharr, G.M. Influences of surface preparation on nanoindentation pop-in in single-crystal Mo. *Scripta Materialia* **2011**, *65*, 469-472.
31. Barnoush, A. Correlation between dislocation density and nanomechanical response during nanoindentation. *Acta Materialia* **2012**, *60*, 1268-1277.

32. Barnoush, A.; Vehoff, H. Recent developments in the study of hydrogen embrittlement: Hydrogen effect on dislocation nucleation. *Acta Materialia* **2010**, 58, 5274-5285.
33. Schuh, C.A.; Mason, J.K.; Lund, A.C. Quantitative insight into dislocation nucleation from high-temperature nanoindentation experiments. *Nat Mater* **2005**, 4, 617-621.
34. Wu, D.; Nieh, T.G. Incipient plasticity and dislocation nucleation in body-centered cubic chromium. *Materials Science and Engineering: A* **2014**, 609, 110-115.
35. Lilleodden, E.T.; Zimmerman, J.A.; Foiles, S.M.; Nix, W.D. Atomistic simulations of elastic deformation and dislocation nucleation during nanoindentation. *Journal of the Mechanics and Physics of Solids* **2003**, 51, 901-920.
36. Njeim, E.K.; Bahr, D.F. Atomistic simulations of nanoindentation in the presence of vacancies. *Scripta Materialia* **2010**, 62, 598-601.
37. Salehinia, I.; Medyanik, S.N. Effects of vacancies on the onset of plasticity in metals-an atomistic simulation study. *Metall Mater Trans A* **2011**, 42A, 3868-3874.
38. Rose, J.; Ferrante, J.; Smith, J. Universal binding energy curves for metals and bimetallic interfaces. *Physical Review Letters* **1981**, 47, 675-678.
39. Rose, J.; Smith, J.; Ferrante, J. Universal features of bonding in metals. *Physical Review B* **1983**, 28, 1835-1845.
40. Rose, J.; Smith, J.; Guinea, F.; Ferrante, J. Universal features of the equation of state of metals. *Physical Review B* **1984**, 29, 2963-2969.

41. Morris, J.R.; Bei, H.; Pharr, G.M.; George, E.P. Size effects and stochastic behavior of nanoindentation pop in. *Physical Review Letters* **2011**, *106*, 165502.
42. Kim, S.M.; Buyers, W.J.L. Vacancy formation energy in iron by positron annihilation. *Journal of Physics F: Metal Physics* **1978**, *8*, L103.
43. Mukherjee, S.; Khraishi, T.; Shen, Y.L. Modeling the effects of particles, interstitials, vacancies and tip geometry on indentation-induced plasticity. *Molecular Simulation* **2006**, *32*, 651-656.
44. Nix, W.D.; Gao, H.J. Indentation size effects in crystalline materials: A law for strain gradient plasticity. *Journal of the Mechanics and Physics of Solids* **1998**, *46*, 411-425.
45. Köhler, B.; Wolff, J.; Franz, M.; Broska, A.; Hehenkamp, T. Investigation of point defect migration in Fe–Al alloys by means of fast doppler broadening technique. *Intermetallics* **1999**, *7*, 269-276.
46. Lund, A.C.; Hodge, A.M.; Schuh, C.A. Incipient plasticity during nanoindentation at elevated temperatures. *Appl Phys Lett* **2004**, *85*, 1362-1364.
47. Mason, J.K.; Lund, A.C.; Schuh, C.A. Determining the activation energy and volume for the onset of plasticity during nanoindentation. *Physical Review B* **2006**, *73*.
48. Schuh, C.A.; Lund, A.C. Application of nucleation theory to the rate dependence of incipient plasticity during nanoindentation. *Journal of Materials Research* **2004**, *19*, 2152-2158.
49. Kim, J.-Y.; Jang, D.; Greer, J.R. Tensile and compressive behavior of tungsten, molybdenum, tantalum and niobium at the nanoscale. *Acta Materialia* **2010**, *58*, 2355-2363.

50. Schaefer, H.E.; Frenner, K.; Wurschum, R. High-temperature atomic defect properties and diffusion processes in intermetallic compounds. *Intermetallics* **1999**, *7*, 277-287.

Figure captions

Fig. 1. Vacancy concentration of Fe-Al alloys based on the experimental approaches (i) [50] , (ii) [26], (iii) [27] , (iv) [27] and (v) [28].

Fig. 2. (a) A defect-free B2 structure. The formation of a mono- vacancy at the Fe sublattice(b), bi-vacancy(c) and a triple defect(d).

Fig. 3 The typical load displacement curves for (a) Fe-30at.%Al and (b) Fe-45at.%Al intermetallics.

Fig. 4 The effect of heat treatment, Al content and loading rate on the the pop-in distribution in (a) Fe-45at.%Al and (b) Fe- 30 at.%Al single crystal.

Fig. 5. The calculated values of maximum shear stress (left Y-axis) and depth of maximum shear stress(right Y-axis) for samples with different Al and vacancy content.

Fig. 6 (a)A graphical representation of the τ_{13} principle shear stress below the surface, as a result of the elastic Hertzian contact between a flat surface and a spherical indent with a contact radius of a (z is the axis of symmetry). (b) The volume of stresses region; (c and d) volume and number of atoms beneath the tip at a defined portion of the maximum shear stress. The lattice parameters were used based on [4].

Fig. 7. The formation of a mono-vacancy at the Fe sublattice in Fe-Al intermetallics with low Al content. Al, Fe and Va show the expected positions of aluminum, iron and vacancies in a B2 or bcc lattices.

Fig. 8. The effect of vacancies on the pop-in load and pop-in width. (a)Fe-30at.%Al samples indented with Berkovich tip,(b) Fe-45at.%Al samples indented with Berkovich tip, (c) Fe-30at.%Al samples indented with conical tip and (d) Fe-45at.%Al samples indented with conical tip.

Fig. 9. (a) The effect of vacancies on the hardness of samples with different Al and vacancy content. (b) predicted and experimental results which show the contribution of the vacancies on the increase of hardness values.

Fig. 10. The effect of heat treatment on the compressive behavior of Fe-30at.%Al macro samples.

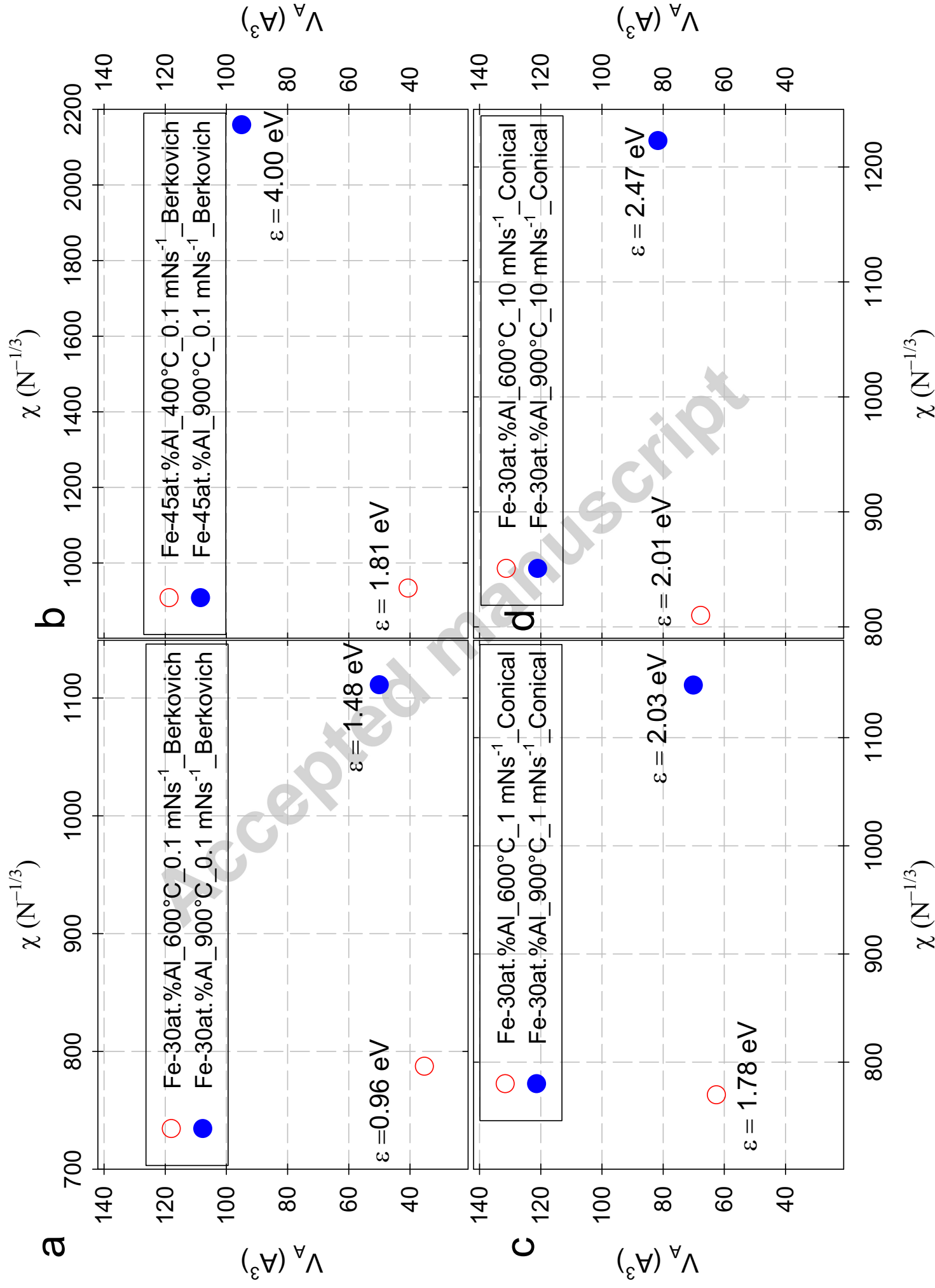
Fig. 11. The linear least-squares procedure used to extract the activation volume of samples with different Al and vacancy content.

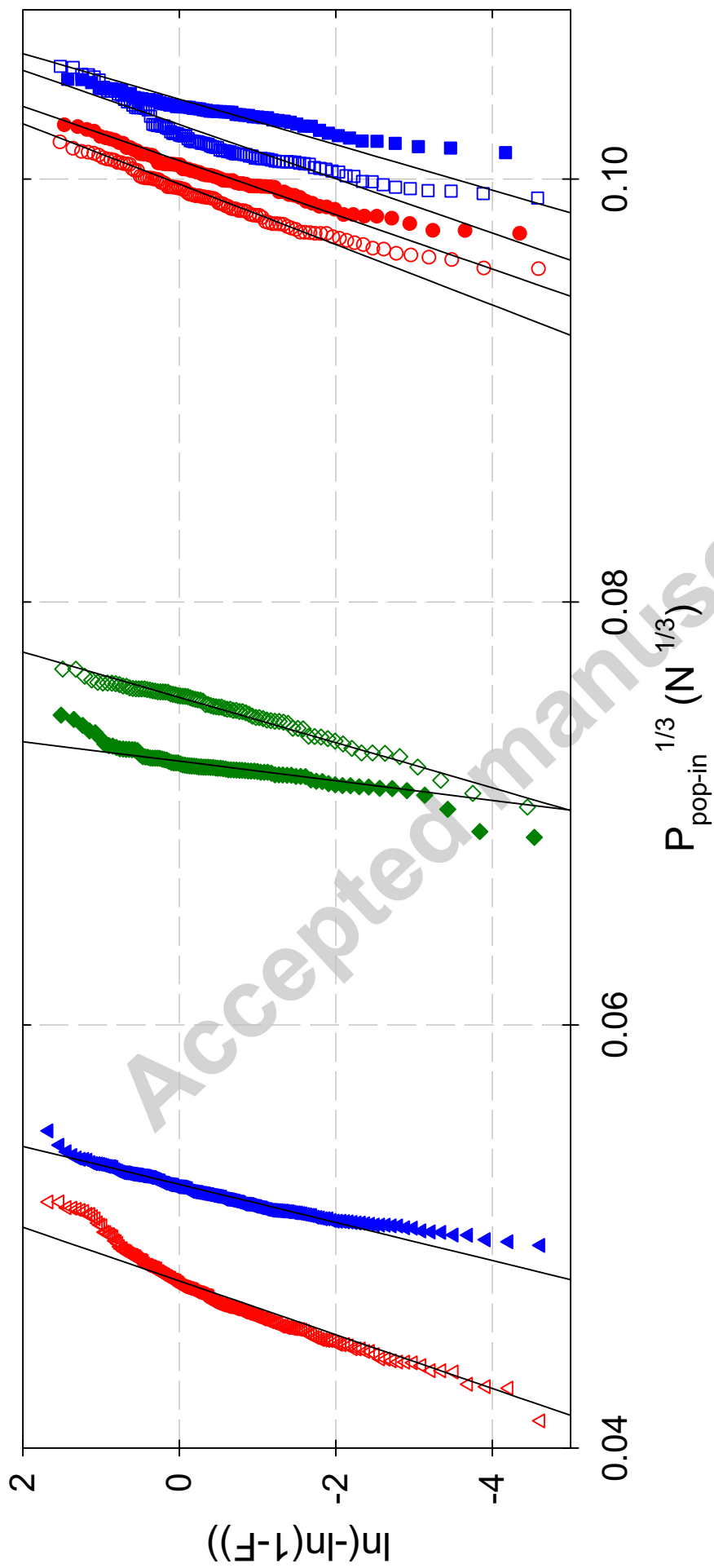
Fig. 12. The activation volume and energy for different samples, quenched from various temperatures. (a) Fe-30at.%Al samples indented with Berkovich tip, (b) Fe-45at.%Al samples indented with Berkovich tip, (c) Fe-30at.%Al samples indented with conical tip with the loading rate of 1mN/s and (d) Fe-30at.%Al samples indented with conical tip with the loading rate of 10 mN/s.

Table captions

Table 1. Type and number of vacancies after each heat treatment in a B2 super lattice [26-28]

<i>Temp.</i> <i>Material</i>	400°C	600°C	900°C
Fe-30 at.%Al	-	mono-vacancies $C_V \approx 8.4 \times 10^{-5}$	mono-vacancies $C_V \approx 1.3 \times 10^{-3}$
Fe-40 at.%Al	triple defects $C_V \approx 1.4 \times 10^{-5}$	-	bi- vacancies $C_V \approx 1.8 \times 10^{-2}$
Fe-45 at.%Al	triple defects $C_V \approx 1.5 \times 10^{-4}$	-	bi-vacancies $C_V \approx \text{n.a.}$





Fe-30Al at.%_Quenched from 600°C_1 mNs⁻¹ Conical tip

Fe-30Al at.%_Quenched from 900°C_1 mNs⁻¹ Conical tip

Fe-30Al at.%_Quenched from 600°C_10 mNs⁻¹ Conical tip

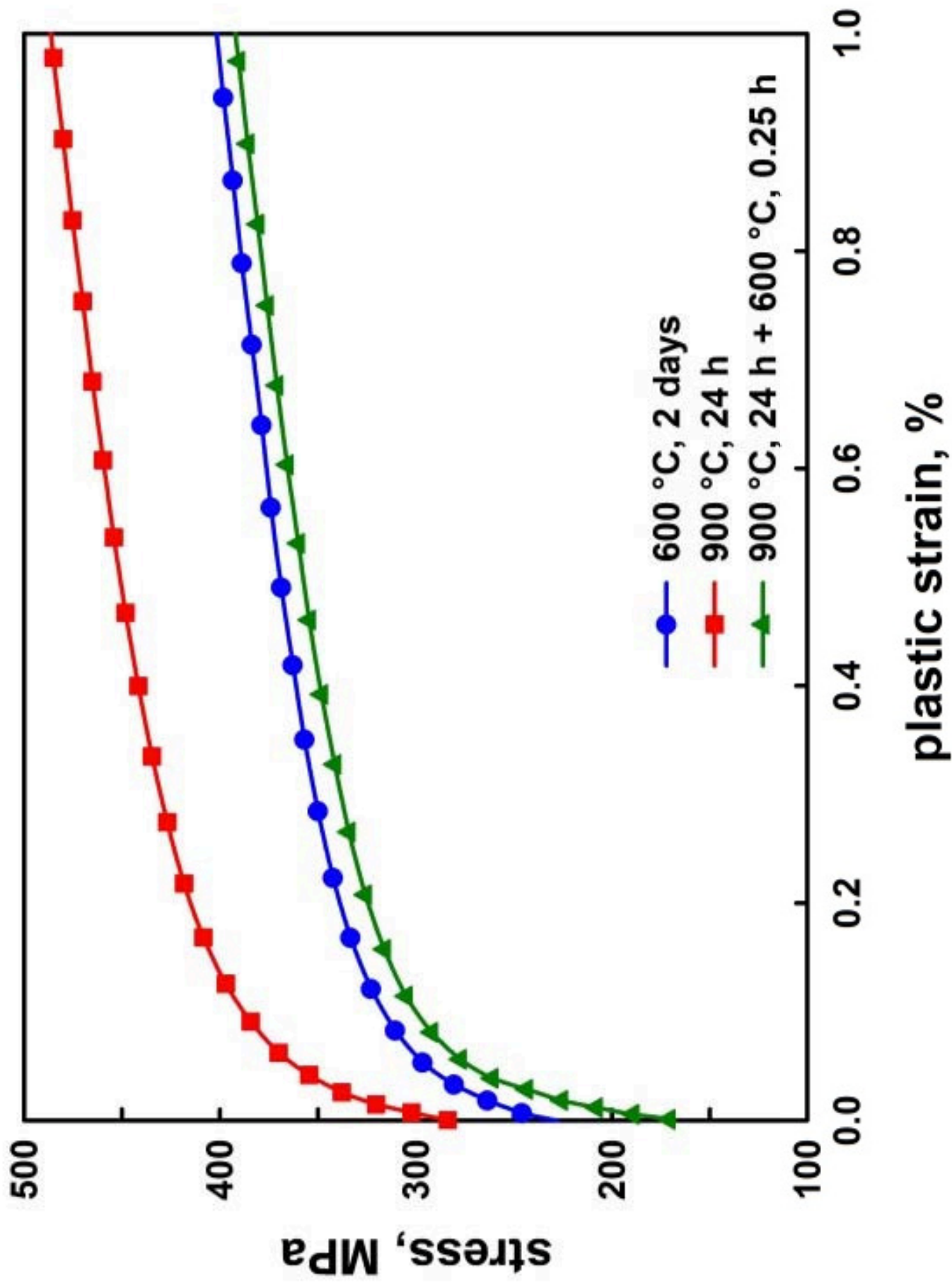
Fe-30Al at.%_Quenched from 900°C_10 mNs⁻¹ Conical tip

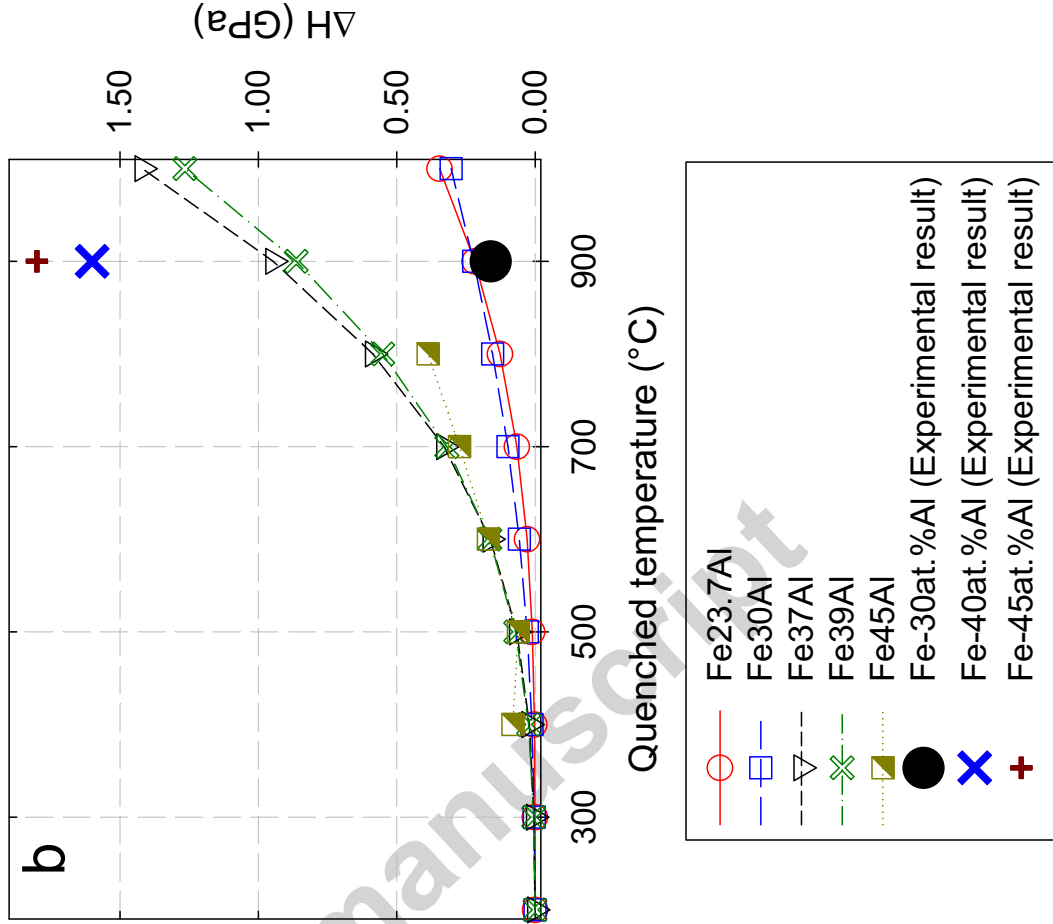
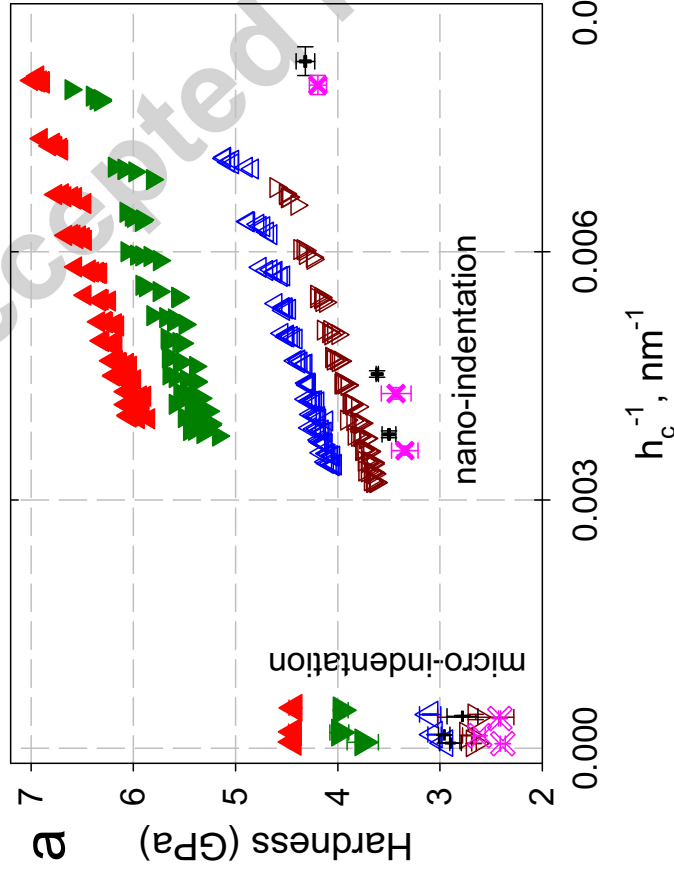
Fe-30Al at.%_Quenched from 600°C_0.1 mNs⁻¹ Berkovich tip

Fe-30Al at.%_Quenched from 900°C_0.1 mNs⁻¹ Berkovich tip

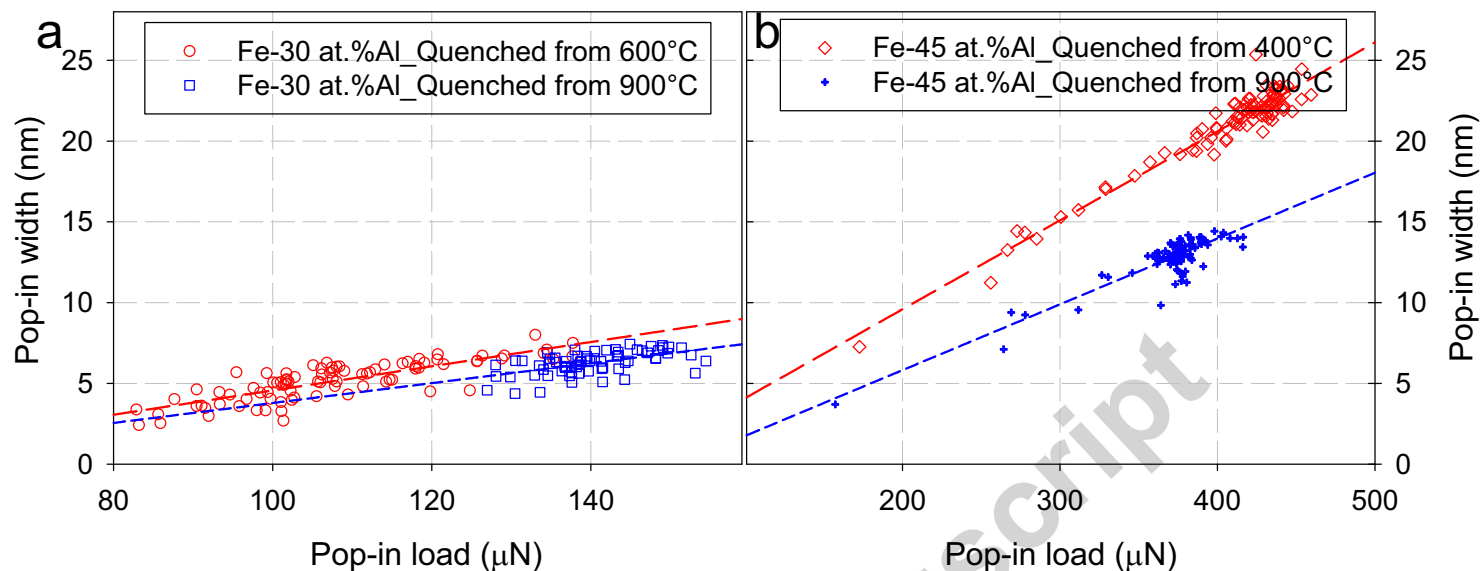
Fe-45Al at.%_Quenched from 400°C_0.1 mNs⁻¹ Berkovich tip

Fe-45Al at.%_Quenched from 900°C_0.1 mNs⁻¹ Berkovich tip





Indented with a sharp Berkovich tip



Indented with a blunt conical tip

